Methodology: Receiver Functions

To interrogate the anisotropic character of the MLD beneath the central U.S., we computed receiver functions at four long-running seismic stations (CCM, WVT, WCI, and BLO) located within the Granite-Rhyolite province. We used the multiple-taper correlation receiver function estimator developed by Park and Levin (2000), which estimates the correlation between the horizontal and vertical component seismograms in the frequency domain. We chose direct P-waves arriving from events with magnitudes M > 5.5 at epicentral distances of 20-100°. All data were visually inspected for strong P-wave arrivals and high-quality horizontal components using EMERALD, an open-source program for processing large data sets (West and Fouch, 2013). We migrate RFs using a simple 1-D velocity model appropriate for continents (AK135; Kennett et al., 1995), using several migration target depths that are subsequently spliced together (this moving-window migration and splicing code, developed by Jeffrey Park and Vadim Levin, is available at http://jparkcodes.blogspot.com/). All RFs were filtered to retain energy at frequencies appropriate for interrogating the lithosphere (high-passed at 0.02 Hz and low-passed at 0.5, 0.75, or 1 Hz). Full receiver function backazimuthal stacks for each station are shown in Figures DR1-4.

Inferring the Orientation of Anisotropy from Receiver Functions

We can distinguish between the possible causes of P-to-SH conversions (i.e., anisotropic structure or dipping interfaces) by looking at backazimuthal variations in transverse component amplitude. For example, anisotropy with a horizontal symmetry axis results in four polarity changes of the Ps phase within the full backazimuthal range, with the signal disappearing at backazimuths parallel and orthogonal to the anisotropic symmetry axis. In contrast, a dipping interface will result in a two-lobed pattern, with SH energy disappearing at backazimuths parallel to the dip of the interface. Anisotropy with a non-horizontal axis of symmetry will result in a mixture of 2- and 4-lobed polarity reversals. However, constraining the plunge of a dipping symmetry axis is largely dependent on P-to-S conversion amplitudes, which are unfortunately not very robust. We note that while tradeoffs such as those between interface depth and isotropic P- and S-wave velocity may affect the interpretation of receiver functions, polarity reversals on transverse component receiver functions are not subject to any tradeoffs. Therefore, the azimuthal orientation of anisotropy represents one of the most robust inferences from anisotropic receiver function analysis.

Most receiver function studies interrogating the MLD make use of S-to-P (Sp) converted phases. S-to-P RFs are advantageous in that the converted P-wave arrives before the parent S-wave and its coda, therefore avoiding contamination by multiples. Unfortunately, characterizing anisotropy using Sp phases requires the determination of the amount of SV versus SH energy of the incoming wave, which is difficult (Frederiksen and Bostock, 2000; Ford, 2013). Because of this, P-to-S (Ps) RF analysis is a superior technique for interrogating anisotropy at precise depths. The interpretation of Ps RFs may be

complicated, however, by the arrival of near-surface multiples around the same time as the converted phases of interest. In order to rule out contamination of the RF signal by reverberations in the time windows examined in this study, we have examined the pulse moveout as a function of epicentral distance (examples are shown in Figures DR5-6). None of the arrivals that we interpret as being due to anisotropy exhibit moveout that is characteristic of near-surface multiples. As long as multiple phases are appropriately accounted for, as we do in this study, Ps RFs are an excellent tool for characterizing sharp changes in anisotropy internal to the lithosphere.

Methodology: Forward Modeling

Software

To generate synthetic seismograms for forward modeling of receiver functions, we use the *raysum* software for creating ray theoretical seismograms in the presence of both dipping interfaces and anisotropy (Frederiksen and Bostock, 2000). While our forward models contain a large number of free parameters that describe several seismic properties, we reiterate that our inferences of the orientation of the anisotropic symmetry axis are the most reliable. Therefore, for simplicity, a number of parameters (described below) are held fixed in our modeling approach.

Isotropic velocities are primarily taken from AK135, with small adjustments (i.e., a velocity drop around the primary MLD pulse) in order to better match the data. Again, however, we do not place any emphasis on the ability of our receiver function analysis to constrain isotropic velocity, especially because of the strong tradeoff that exists between layer thickness and P- and S-wave velocities. We assume hexagonally symmetric anisotropy, with the strength of anisotropy held fixed at 3%. We find that 3% anisotropy roughly matches the amplitude of P-to-SH conversions in the actual data, and since Ps phase amplitude is one of the least robust components of a receiver function, we do not attempt to further constrain the precise strength of anisotropy. P- and S-wave anisotropies are always chosen to be the same, in line with previous studies (e.g., Park et al., 2004; Nikulin et al., 2009). The definition of the anisotropy parameter, η, which controls the propagation velocity for directions other than parallel and perpendicular to the anisotropic symmetry axis, is modified from the original *raysum* code. This modification allows a direct comparison between the *raysum* code and synthetic receiver functions generated using the *anirec* code used by Levin and Park (1997, and later), by requiring that the 3-D expression of velocity be purely ellipsoidal. We refer the reader to a detailed explanation of this in Sherrington et al. (2004), Appendix A. Finally, we note that the *raysum* code uses one representative slowness for each backazimuthal angle, which we choose to be the average epicentral distance from our actual events in each backazimuthal bin.

Grid Searches

Our first grid search utilized the simplest scenario: one mid-lithospheric discontinuity dividing an anisotropic lower and upper lithosphere. Using this model, we performed a search over all possible azimuths and plunges of the anisotropic symmetry axis in each of

these two layers. However, we found that a two-layer model could not accurately portray our RF observations; therefore, we elected to use three layers of anisotropy in subsequent modeling. A justification for this choice is illustrated in Figure DR7, which shows the predicted Ps conversions for a model with either two or three layers of anisotropy. In receiver functions derived from actual data, the time span between 5-10 sec after the P-wave arrival exhibits roughly three distinct pulses. A 2-layer model of the mantle lithosphere produces only two pulses in this 5 sec window (i.e., one from the conversion at the MLD and one at the Moho). However, a model with three distinct anisotropic layers internal to the lithosphere results in roughly three Ps phases within a 5 sec time window, matching the features of the actual data. Adding additional layers to the model will always improve the fit to the data but risks over-parameterizing the problem; therefore, we do not advocate for anything more complex than a model with three anisotropic layers, although our data does not preclude this.

Our second set of grid searches used three layers of anisotropy; we performed grid searches for the best-fitting orientation of anisotropy in upper lithospheric layers UL1 and UL2. This grid search was more refined, using a 10° spacing in azimuthal orientation of anisotropy. We also experimented with using a slow axis of symmetry and found that the results are very similar to a fast axis (except 90° out of phase), due to the near-horizontal orientation of the anisotropic symmetry axis. We tested models with a modest dip for the MLDs (~10°), but find that its influence is minimal. Finally, using the best-fitting trend and plunge for anisotropy in layers UL1 and UL2, we tested various orientations (trend and plunge) of anisotropy in the lower (and less well constrained) lithospheric layer.

Grid search models were evaluated quantitatively and compared using a chi-squared measure for best fit, where

$$\chi^2 = \sum \frac{\left(X_{Data} - X_{Model}\right)^2}{\sigma^2},$$

with the value of σ set to an "expected" or "acceptable" value for misfit. Based on the amplitude of our actual receiver functions, we always chose σ = 0.1. However, we note that in this simple case of using our definition of chi-squared to simply compare misfits and always holding σ constant, the value of σ (which would be more meaningful when using a Metropolis algorithm or similar to explore model space; Metropolis, 1953) is not important.

The location and timing of transverse component polarity reversals based on our best-fit model and actual data are compared in Figure DR8. Here we compare the model predictions not only to station WCI, which was the basis for developing the model, but also to stations BLO, CCM, and WVT. Our model matches polarity reversals stemming from upper lithospheric structure at all stations (i.e., at ~75-90 km, negative/red polarities in the NW and SE quadrants and positive/blue polarities in the NE and SW quadrants), reflecting a well-constrained N- to NW-orientation of anisotropy in the upper mantle lithosphere throughout our study area. At depths below ~100 km, the quality of the match between our preferred model and actual data begins to degrade, and we do not interpret the anisotropic geometry inferred at these depths. We note, however, that at ~100-115 km,

we see at least some evidence of positive polarity phases at northern backazimuths and negative polarity phases at southern backazimuths at all stations.

Dipping Interfaces

It is worth commenting further on the possibility of dipping structure beneath the receivers and its possible influence on our interpretations. One of the most straightforward ways to infer the presence of dipping interfaces is an arrival at 0 sec time delay on transverse component receiver functions (i.e., from the bending of the direct P-wave out of the source-receiver plane). In this scenario, polarity reversals will occur parallel to the dip of the structure (i.e., 180° apart). An examination of the character of the transverse component arrivals at 0 sec time delay (Figures DR1-DR4) reveals differences among the stations, making a unified interpretation difficult. Station BLO exhibits little or no energy on transverse component receiver functions at zero time lag, arguing for flat layers. Zero time delay arrivals for station WCI are essentially all positive (with the exception of the150-200° backazimuthal range, which exhibits no energy arriving at zero time lag). Similarly, station WVT has mostly positive energy at zero time lag on the transverse component, with polarity reversals occurring at backazimuths of 40° and 300°, far from the 180° periodicity that would be expected for a dipping interface. It is possible that these zero time delay arrivals may arise from scattering of the direct P-wave due to heterogeneous structure in the crust. Station CCM is the only station that exhibits zero time lag energy that is clearly consistent with dipping structure. Polarity reversals occur at ~110° (positive to negative) and ~300° (negative to positive) backazimuths, essentially 180° periodicity. This pattern in polarity indicates the likely presence of an eastward dipping interface, and is a mirror image to the strong transverse component polarity arrivals at ~1 sec. Therefore, this likely corresponds to an eastward dipping structure in the upper crust.

Uncertainty Estimates

To ensure the features that we interpret are robust, we performed jackknife uncertainty estimates on all bin-summed receiver functions, as shown in Figure DR9. The jackknife approach computes receiver function estimates on subsets of the data (i.e., throwing out one data point at a time), allowing for an estimate of the uncertainty in the data based on the scatter among subsets. We performed jackknife uncertainty estimates on each backazimuthal bin-averaged set of receiver functions for all stations used in this study (Figure DR9), which demonstrate that the P-to-S conversions that we interpret are robust features of the data. [We note parenthetically that unlike the moving-window migration and splicing technique used to compute RFs elsewhere in the paper (see DR section on "Methodology: Receiver Functions"), in order to make the jackknife resampling computationally tractable we only migrate to one specific target depth (90 km) when computing jackknife uncertainties. This results in some apparent moveout of the direct P-wave arrival in Figure DR9.] We further emphasize that the consistency of apparent P-to-S conversions across several different backazimuths (Figures DR1-DR4), as well as the large number of individual receiver functions that contribute to most bin-average stacks (in which random noise would not stack coherently), also suggest that our receiver function observations are robust.

In order to assess the robustness of our estimates of the best-fitting model parameters shown in Figure 5 and Table DR1, we created contour plots of model fitness as a function of the trend and plunge of anisotropy in each layer. Examples of these contour plots for parameter sensitivity are shown in Figure DR10. Figure DR10a shows model fitness values as a function of the trends of anisotropy in upper lithospheric layers 1 and 2 (UL1 and UL2, respectively). For this particular example, there is no anisotropy in the lower lithosphere, and the plunge of the anisotropic symmetry axes in both layers is held constant at 15° (although a similar contour plot for anisotropy with zero plunge appears nearly identical). The nearly ~180° periodicity in areas of good model fit is a result of the nearly horizontal anisotropic symmetry axes. For the case of a 15° plunge of the anisotropic symmetry axes, a N- to NW-orientation of anisotropy in both layers provides the best fit to the data, and is apparently well-constrained (to within ~25°). Similarly, Figure DR10b shows model fitness values as a function of the trend and plunge of anisotropy in the lowermost lithosphere. Parameters for the trend and plunge of the anisotropic symmetry axes in UL1 and UL2 are held at their maximum values from Figure DR10a. At time delays corresponding to arrivals converted at lower lithospheric depths, the transverse component arrivals at station WCI (Figure DR1) appear to be roughly two-lobed in character, implying a strong plunge of the anisotropic symmetry axis out of the horizontal plane. This is best approximated by a roughly eastward directed (~40-110°) anisotropic symmetry axis with a plunge of ~50-60°; however, the contour plot indicates that this parameter is not as well constrained by the data as those explored in Figure DR10a.

References for Data Repository

Ford, H.A.W., 2013, A seismological perspective on the lithosphere-asthenosphere boundary [Ph.D. thesis]: Brown University.

Frederiksen, A.W., and Bostock, M.G., 2000, Modelling teleseismic waves in dipping anisotropic structures: Geophysical Journal International, v. 141, p. 401–412.

Kennett, B. L. N., Engdahl, E. R., and Buland, R., 1995, Constraints on seismic velocities in the Earth from traveltimes: Geophysical Journal International, v. 122, p. 108-124.

Levin, V., and Park, J., 1997, P-SH conversions in a flat-layered medium with anisotropy of arbitrary orientation: Geophysical Journal International, v. 131, p. 252-266, doi:10.1111/j.1365-246X.1997.tb01220.x.

Metropolis, N., Rosenbluth, A. W., Rosenbluth, M. N., Teller, A. H., and Teller, E., 1953. Equation of state calculations by fast computing machines: Journal of Chemical Physics, v. 21, p. 1087-1091.

Nikulin A., Levin, V., and Park, J., 2009. Receiver function study of the Cascadia megathrust: Evidence for localized serpentinization: Geochemistry, Geophysics, Geosystems, v. 10, Q07004, doi:10.1029/2009GC002376.

Park, J., and Levin, V., 2000, Receiver functions from multiple-taper spectral correlation estimates: Bulletin of the Seismological Society of America, v. 90, p. 1507-1520.

Park, J., Yuan, H. Y., and Levin, V., 2004. Subduction zone anisotropy beneath Corvallis, Oregon: A serpentinite skid mark of trench-parallel terrane migration?: Journal of Geophysical Research, v. 109, B10306, doi:10.1029/2003JB002718.

Sherrington, H. F., Zandt, G., and Frederiksen, A., 2004. Crustal fabric in the Tibetan Plateau based on waveform inversions for seismic anisotropy parameters: Journal of Geophysical Research, v. 109, B02312, doi:10.1029/2002JB002345.
West, J. D., and Fouch, M. J., 2012, EMERALD: A Web Application for Seismic Event Data Processing: Seismological Research Letters, v. 83, p. 1061-1067.

Figure DR1. Radial (left) and transverse (right) component receiver function results for station WCI. RFs are plotted as a function of time, with 0 sec being the arrival of the P-wave at the seismic station, and grouped by backazimuth. In general, positive/blue (negative/red) pulses represent a velocity increase (decrease) with depth. RFs are low-passed at 1 Hz. Solid black line marks the arrival of Ps phases converted at the Moho, while the dashed green line represents the most coherent conversion from mid-lithospheric structure. Unshaded regions highlight the arrival of negative polarity phases that are converted at mid-lithospheric depths.

Figure DR2. Receiver function results for station BLO. Plotting is as described in Figure DR1.

Figure DR3. Receiver function results for station WVT. Plotting is as described in Figure DR1.

Figure DR4. Receiver function results for station CCM. Plotting is as described in Figure DR1.

Figure DR5. Receiver functions from station WCI, binned and stacked by epicentral distance and low-passed at 1 Hz. Left and right panes show receiver functions from events at 0-70° and 300-350° backazimuths, respectively. Green lines denote direct conversions from sharp interfaces, while orange lines indicate multiple phases. Colored lines are plotted as solid for pulses that have an identifiable origin. As epicentral distance increases, the delay time of a Ps phase will decrease (i.e., as the wave arrives at a steeper incidence angle), while the delay time of a multiple phase will increase.

Figure DR6. Receiver functions from station CCM, binned and stacked by epicentral distance and low-passed at 1 Hz. Left and right panes show receiver functions from events at 150-170° and 310-360° backazimuths, respectively. Plotting conventions are as in Figure DR5.

Figure DR7. Examples of a subset of receiver functions for (a) station WCI, (b) a model with two anisotropic layers, and (c) a model with three anisotropic layers. Dashed boxes denote time windows of length ~5 sec, for which we attempt to match the frequency of pulse occurrence.

Figure DR8. Transverse component RF polarity patterns at four different time intervals (corresponding to depths internal to the lithosphere), plotted as described in Figure 3. The average depth and corresponding Ps delay time (*dt*) of each slice is given to the left. For

stations BLO, WVT, and CCM, the matching transverse component polarity pattern was sometimes slightly offset in time, and therefore the *dt* of the time slice is given in the center of the pole plot. Orange boxes enclose transverse component receiver functions that exhibit similar polarity reversal patterns to our preferred model. The strongest similarities among stations and the model are seen in the shallow mantle lithosphere (~7-10 sec, top two rows of transverse component RFs), for which we infer a N- to NW-orientation of the anisotropic symmetry axis.

Figure DR9. Jackknife uncertainties (green shaded regions) for receiver functions computed at all stations (compare to Figures DR1-4). Blue and red pulses that are still clearly identifiable are robust according to the jackknife estimates. To make the jackknife resampling process computationally tractable, these RFs were computed by migrating to only one specific target depth (90 km, now at time = 0 sec) close to the arrival of P-to-S conversions from mid-lithospheric discontinuities. This results in slight moveout of the direct P-wave arrival (now at times of -9 to -10 sec) compared to Figures DR1-4. Vertical green dashed lines represent the most coherent radial component conversion from mid-lithospheric structure, as plotted in Figures DR1-4. The number of receiver functions stacked in each backazimuthal bin is shown in gray along the right side of the figures.

Figure DR10. (a) Contour plot of model fitness as a function of the trend of the anisotropic symmetry axes in upper lithospheric layers 1 and 2 (i.e., UL1 and UL2). For this particular example, the plunge of the symmetry axes is held constant at 15° and the lithosphere below these layers is isotropic. (b) Contour plot of model fitness as a function of the trend and plunge of anisotropy in the lowermost lithospheric layer. For this plot, anisotropic parameters for the upper lithospheric layers are held constant at the values that produced the highest fitness values in (a).

Table DR1. Model parameters used to describe the model shown in Figure 5 and generate synthetic receiver functions shown in Figure 4. Although we only test for variations in the orientation of anisotropy across boundaries (bold font), these discontinuities may additionally correspond to an offset in isotropic velocity. P- and S-wave anisotropy are held constant at 3%, which results in RFs that roughly match the amplitudes of P-to-SH arrivals in the actual data.

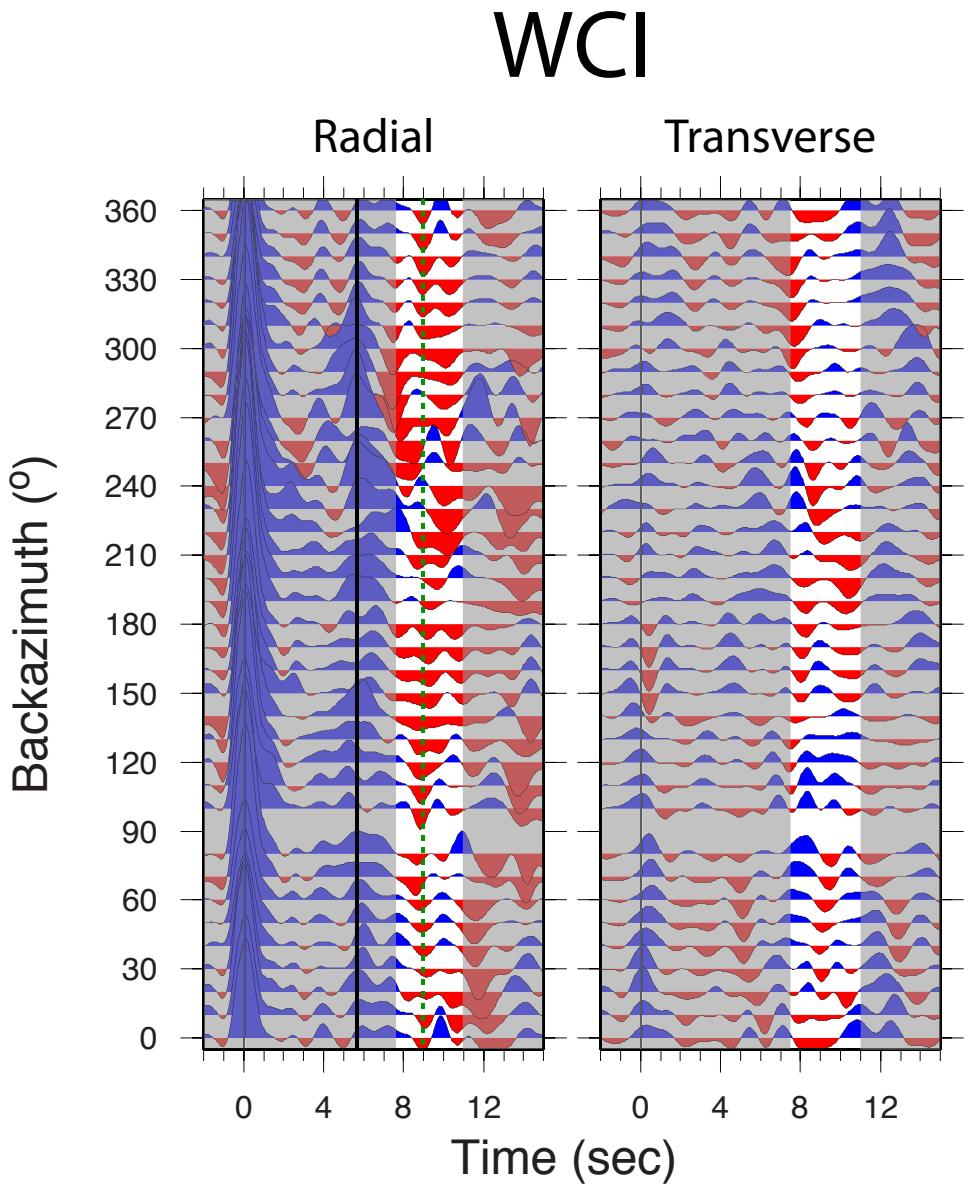
WCI
Radial
Transverse
Backazimuth (°)
360
330
300
270
240
210
180
150
120
90
60
30
0
0
4
8
12
0
4
8
12
Time (sec)

Figure DR1

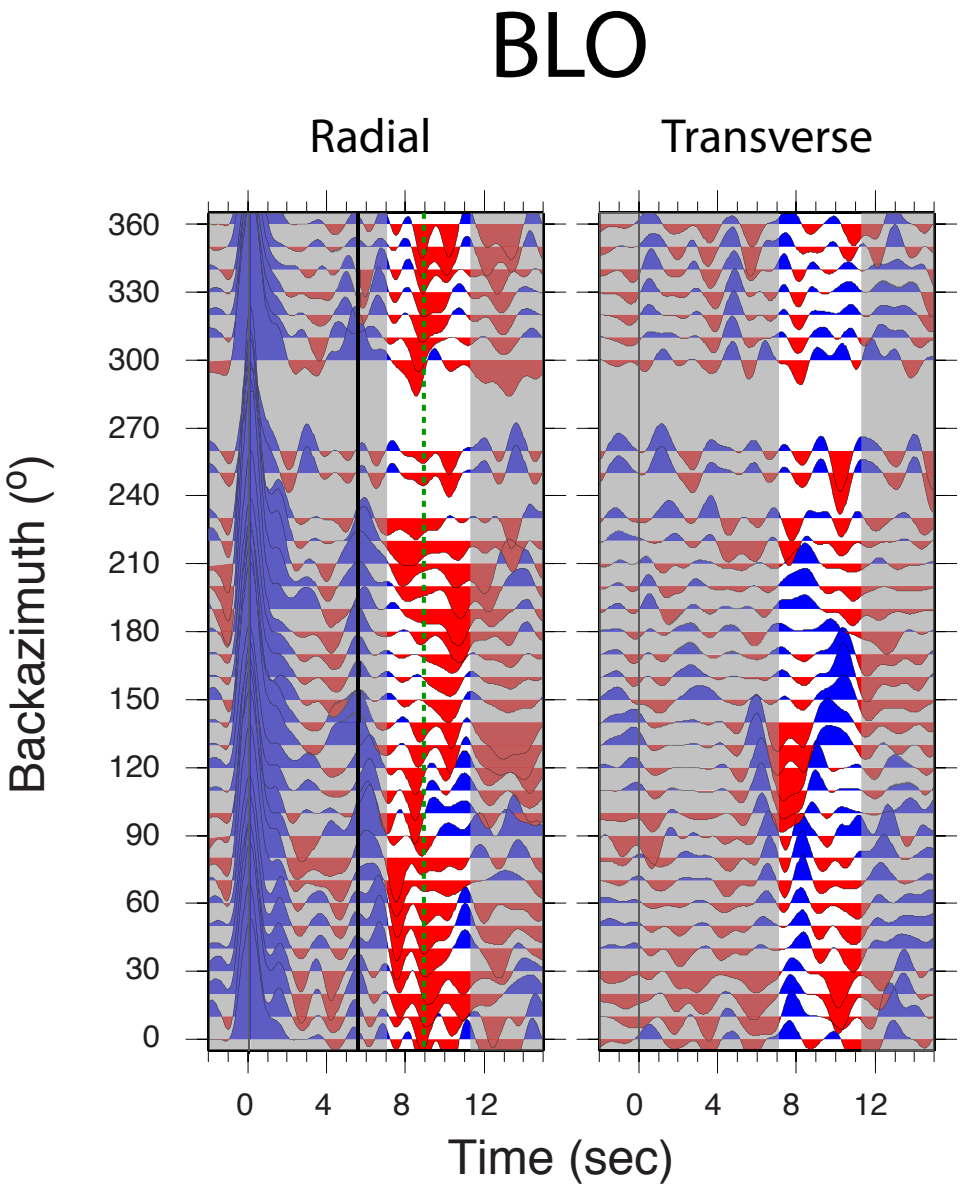
BLO
Radial
Transverse
Backazimuth (°)
360
330
300
270
240
210
180
150
120
90
60
30
0
0
4
8
12
0
4
8
12
Time (sec)

Figure DR2

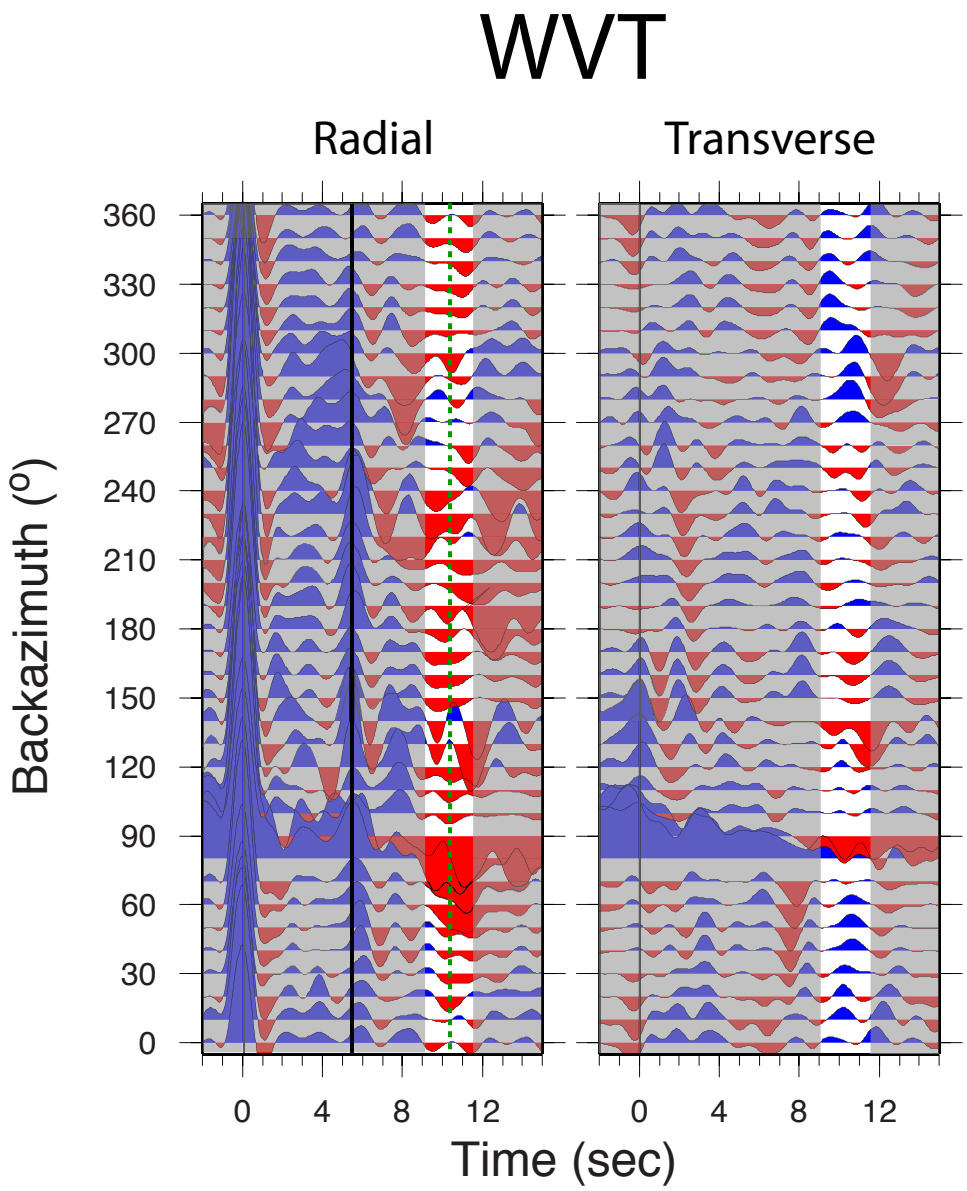
WVT
Radial
Transverse
Backazimuth (°)
360
330
300
270
240
210
180
150
120
90
60
30
0
0
4
8
12
0
4
8
12
Time (sec)

Figure DR3

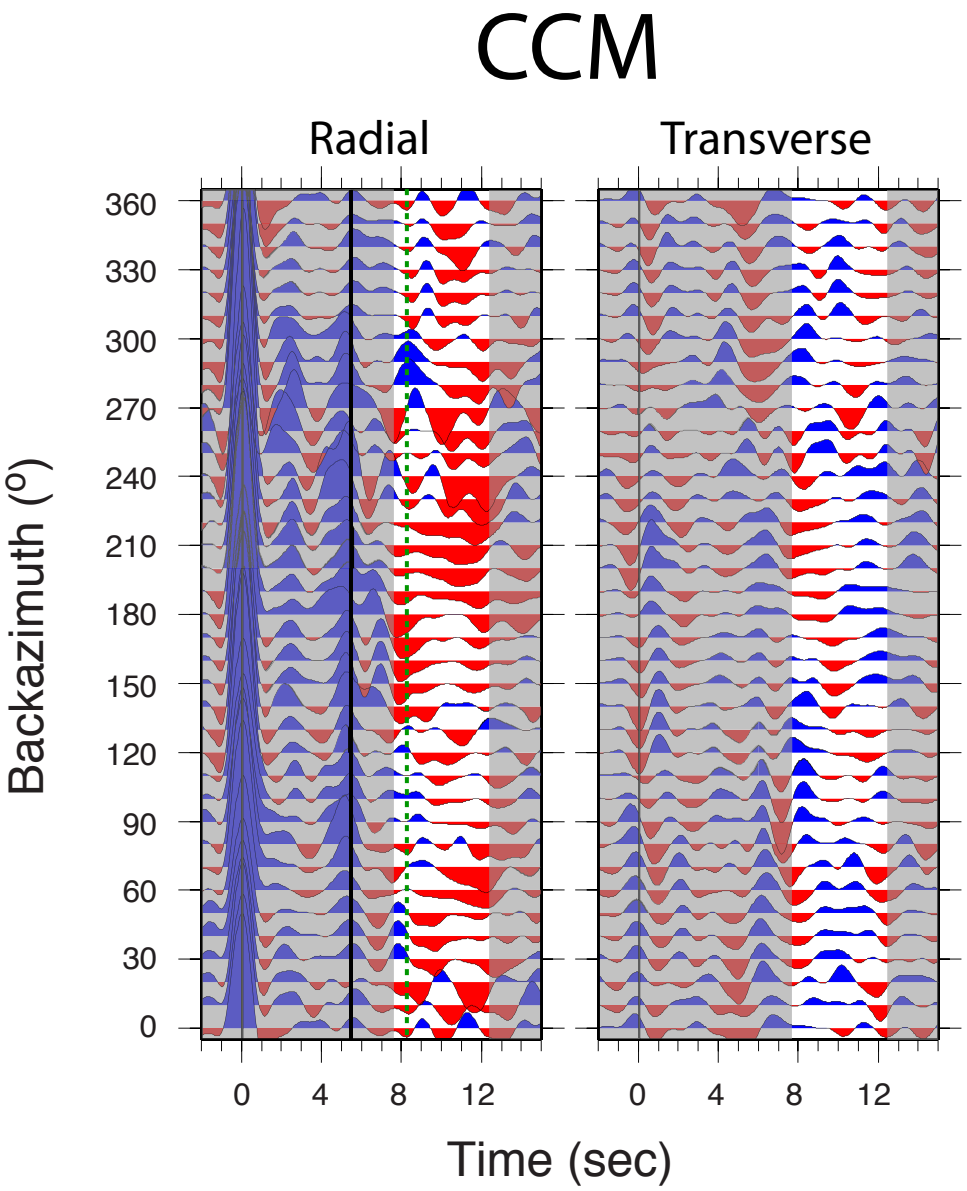
CCM
Radial
Transverse
Backazimuth (°)
360
330
300
270
240
210
180
150
120
90
60
30
0
0
4
8
12
0
4
8
12
Time (sec)

Figure DR4

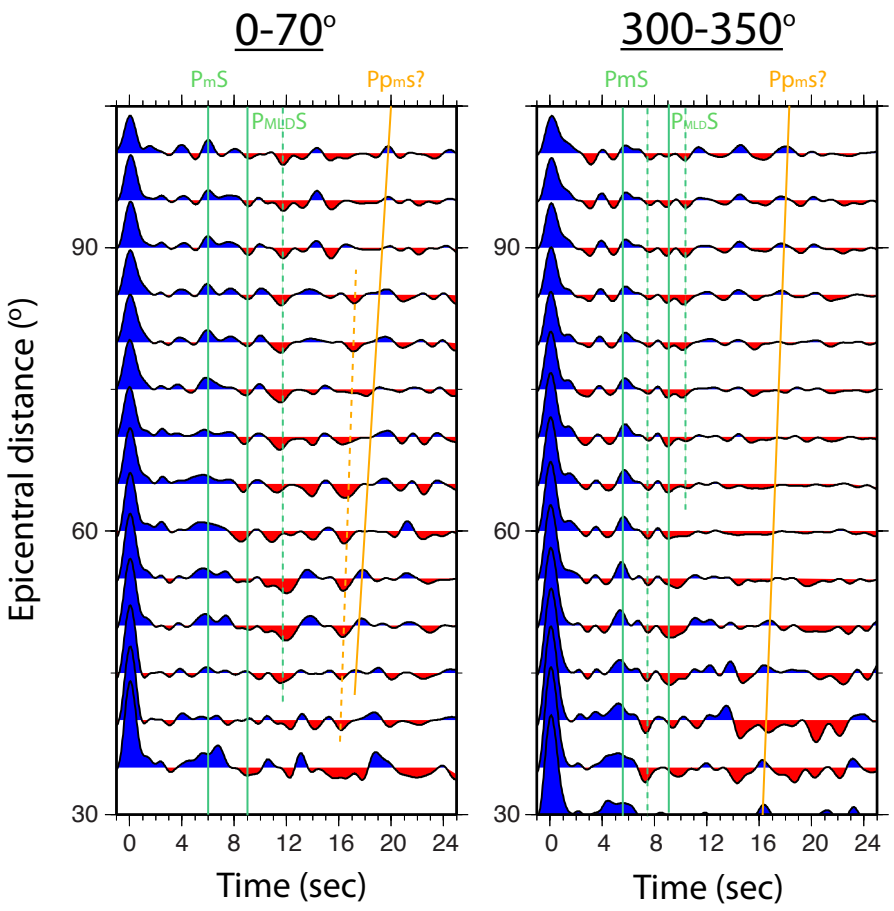
0-70°
300-350°
PmS
Ppms?
PMLDS
90
60
30
Epicentral distance (°)
0
4
8
12
16
20
24
Time (sec)

Figure DR5

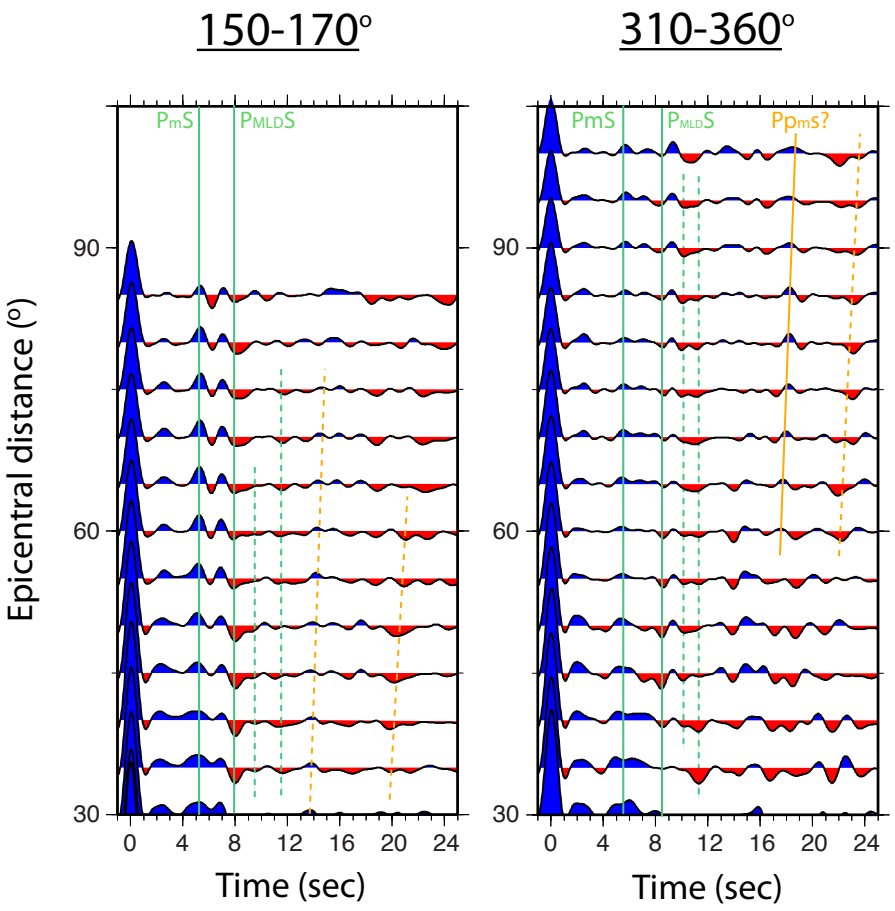
150-170°
310-360°
PmS
PMLDS
PpmS?
Epicentral distance (°)
90
60
30
0
4
8
12
16
20
24
Time (sec)

Figure DR6

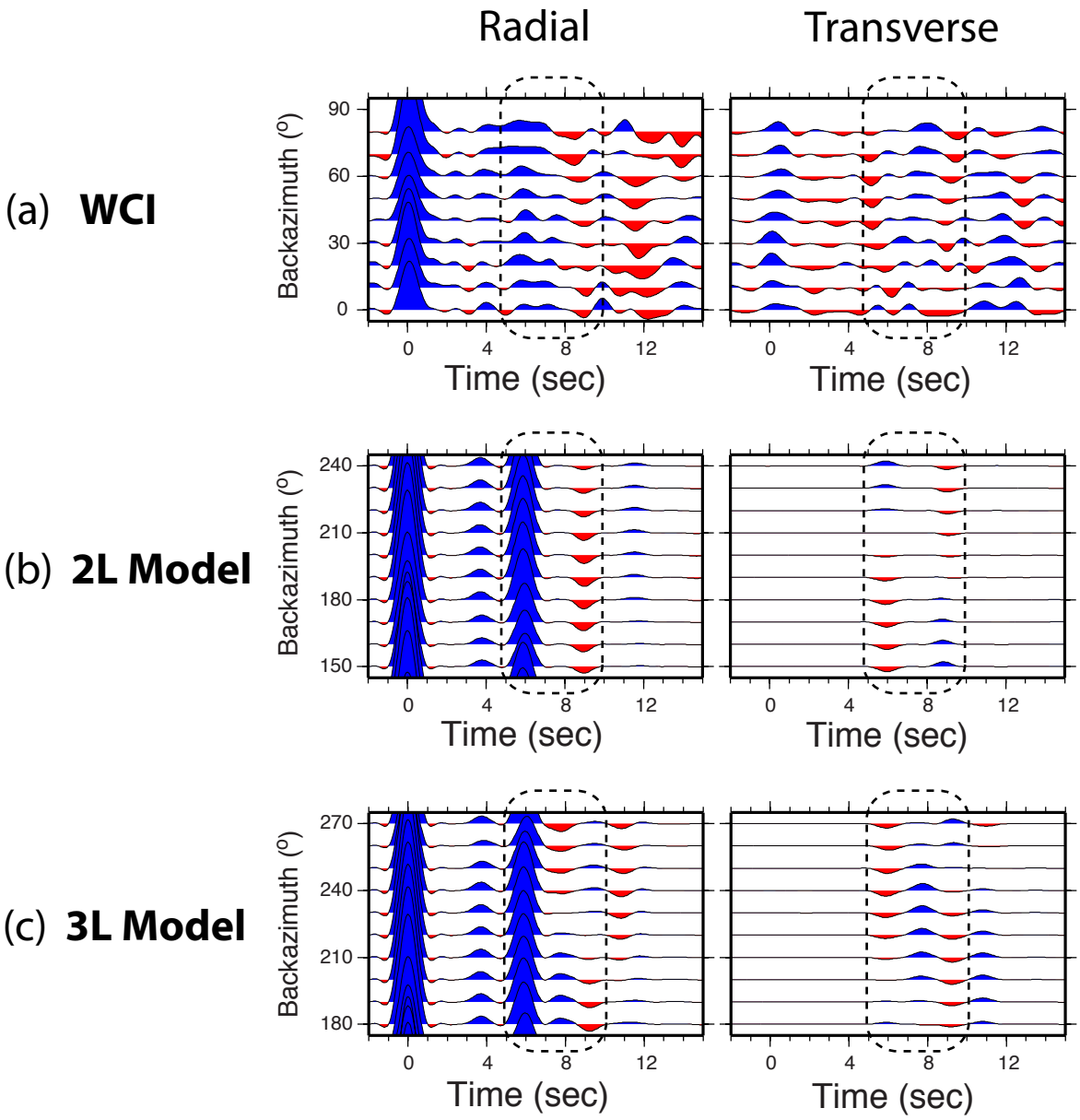
Radial
Transverse
(a) WCI
(b) 2L Model
(c) 3L Model
Backazimuth (°)
90
60
30
0
240
210
180
150
270
0
4
8
12
Time (sec)

Figure DR7

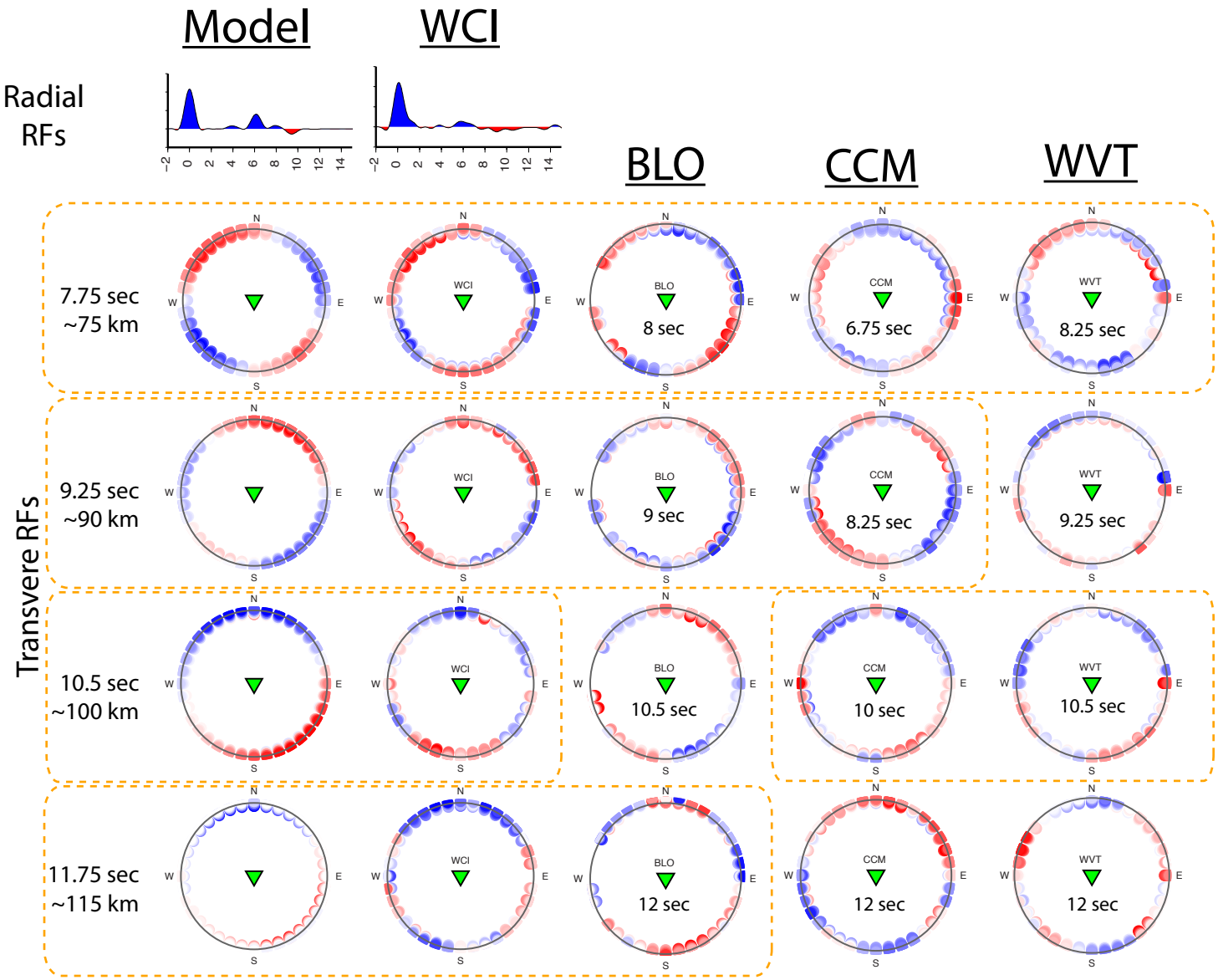
Model
WCI
Radial RFs
BLO
CCM
WVT
Transvere RFs
7.75 sec ~75 km
9.25 sec ~90 km
10.5 sec ~100 km
11.75 sec ~115 km
8 sec
6.75 sec
8.25 sec
9 sec
8.25 sec
9.25 sec
10.5 sec
10 sec
10.5 sec
12 sec
12 sec
12 sec

Figure DR8

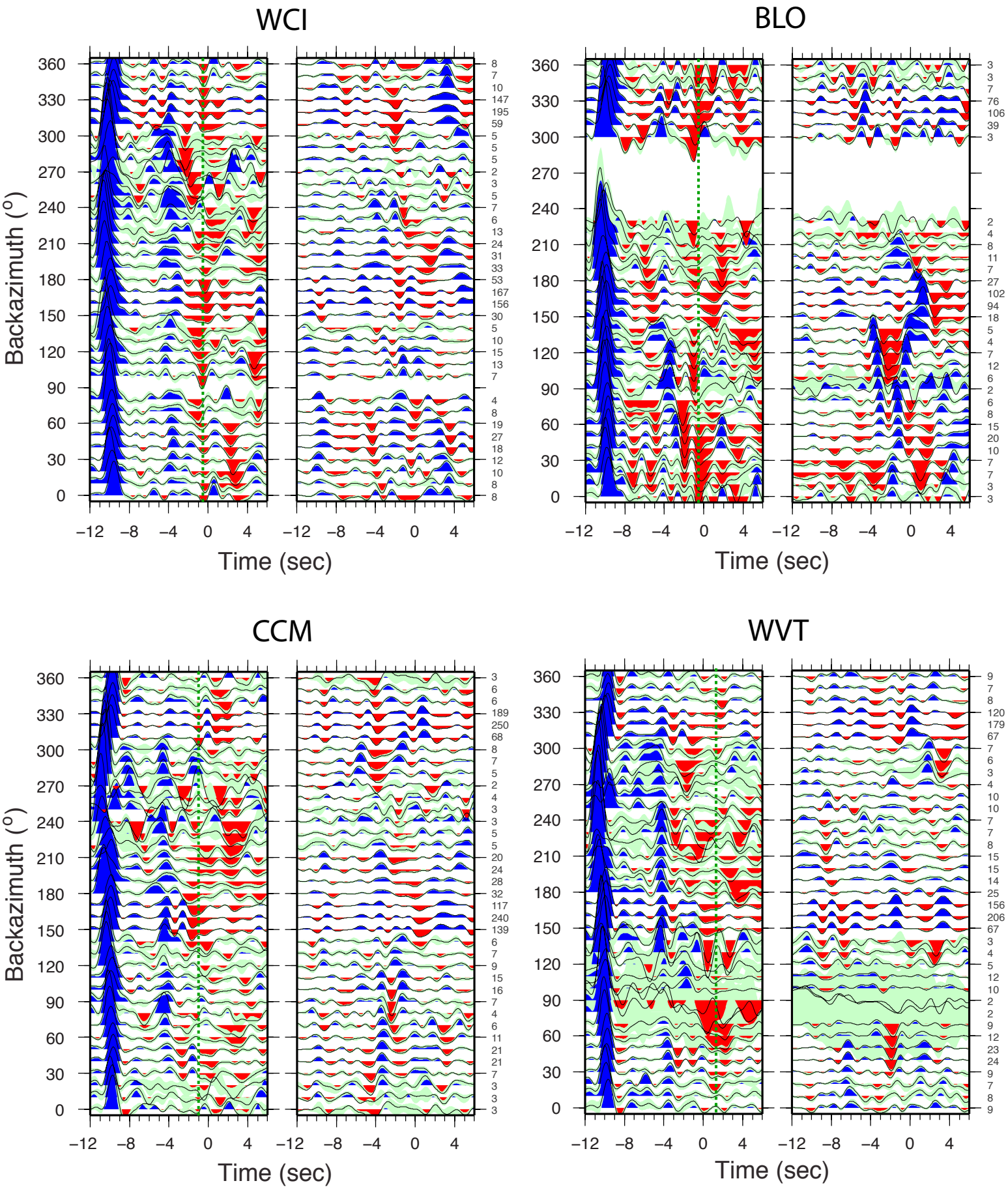
WCI
BLO
CCM
WVT
Backazimuth (°)
Time (sec)
0
30
60
90
120
150
180
210
240
270
300
330
360
−12
−8
−4
0
4

Figure DR9

(a)

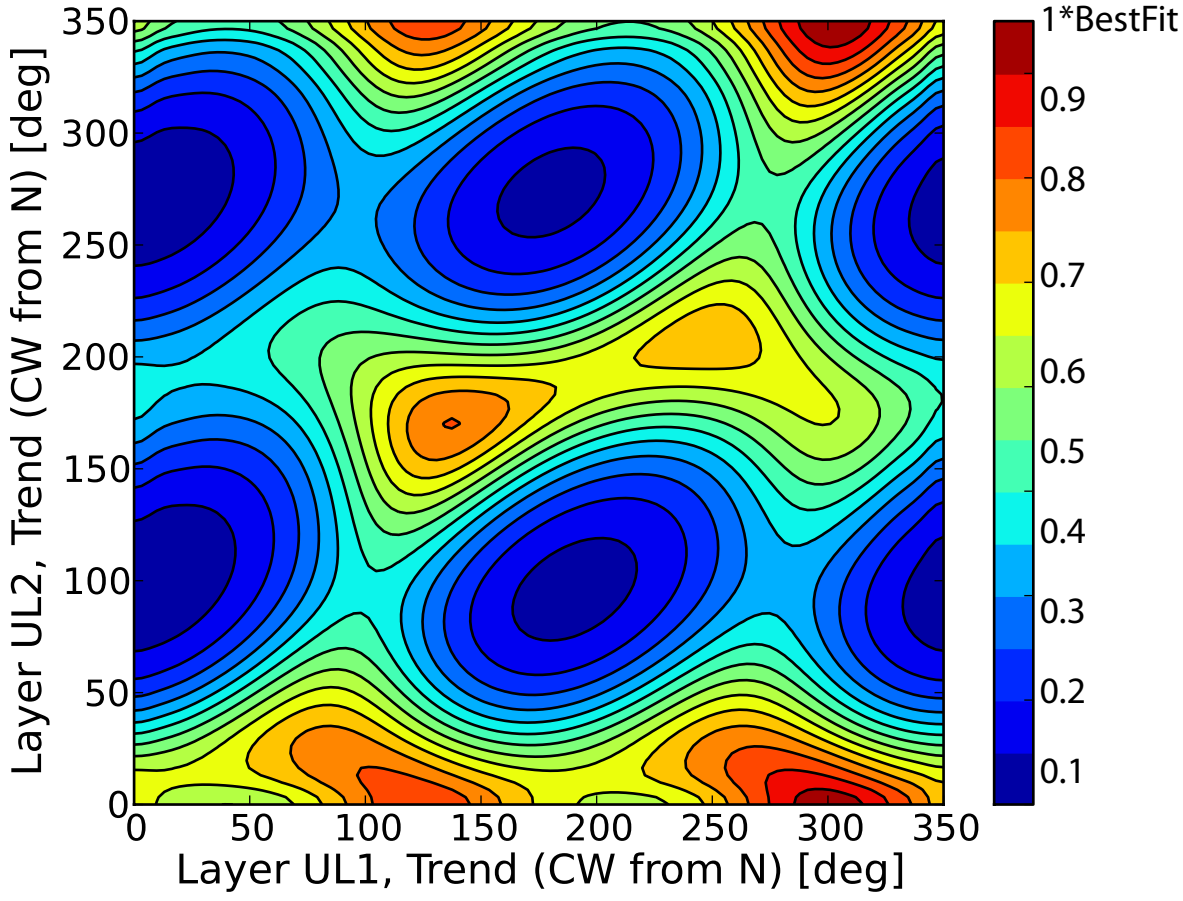

(b)

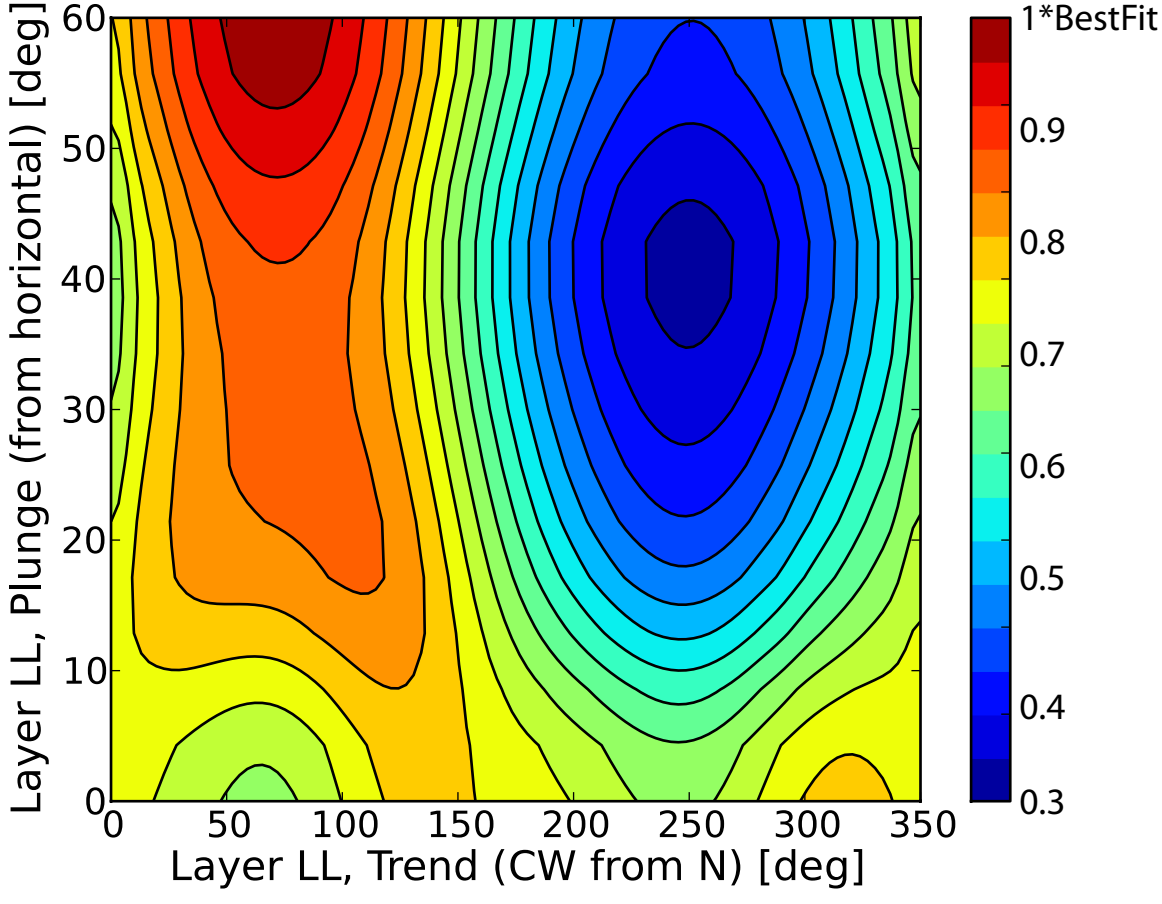

Figure DR10

Table DR1. Best Fit Model for Station WCI

Depth (m)	V_P (m/s)	V_S (m/s)	ρ (g/cm^3)	% anisotropy	θ (°)	φ (°)
32000	5800	3400	2700	—	—	—
50000	6470	3650	3000	—	—	—
70000	8040	4800	3502	3	**300**	**15**
90000	8040	4800	3502	3	**350**	**15**
110000	7900	4650	3427	3	**70**	**60**
200000	7900	4650	3427	—	—	—
	7800	4600	3400	—	—	—

"Depth" refers to the depth of the bottom of the layer
θ = azimuth from north of anisotropic symmetry axis
φ = plunge from horizontal of anisotropic symmetry axis
% anisotropy refers to both P- and S-wave anisotropy